Chemical Science

ROYAL SOCIETY OF CHEMISTRY

EDGE ARTICLE

View Article Online
View Journal | View Issue

Check for updates

Cite this: *Chem. Sci.*, 2024, **15**, 10200

All publication charges for this article have been paid for by the Royal Society of Chemistry

Open Access Article. Published on 22 May 2024. Downloaded on 2/25/2026 8:18:42 AM. This article is licensed under a Creative Commons Attribution-NonCommercial 3.0 Unported Licence.

A quasi-solid-state self-healing flexible zinc-ion battery using a dual-crosslinked hybrid hydrogel as the electrolyte and Prussian blue analogue as the cathode material†

Jiawei Long, [a] Tianli Han,[a] Xirong Lin,[b] Yajun Zhu,[ac] Jinyun Liu*[a] and Junjie Niu *[d]

Received 9th April 2024
Accepted 20th May 2024

DOI: 10.1039/d4sc02348j

rsc.li/chemical-science

Due to their excellent safety and lower cost, aqueous Zn-ion batteries (AZIBs) have garnered extensive interest among various energy-storage systems. Here we report a quasi-solid-state self-healing AZIB by using a hybrid hydrogel which consists of dual-crosslinked polyacrylamide and polyvinyl alcohol as a flexible electrolyte and a cobalt hexacyanoferrate ($K_{3.24}Co_3[Fe(CN)_6]_2 \cdot 12.6H_2O$) Prussian blue analogue as the cathode material. The obtained hybrid hydrogel showed a superhigh fracture strain of up to 1490%, which was almost 15 times higher than that of the original size. Due to the fast formation of hydrogen bonds, the self-healed hydrogel from two pieces still displayed 1165% strain upon failure. As a result, the self-healed battery delivered stable capacities of 119.1, 108.6 and 103.0 mA h g^{-1} even after being completely cut into 2, 3 and 4 pieces, respectively. The battery capacity recovery rates for each bending cycle exceeded 99.5%, 99.8%, 98.6% and 98.9% during four continuous bending cycles (30 times bending at 90° for each cycle), which indicates outstanding flexibility and self-healing capability. In parallel, the hydrogel electrolyte displayed a broader electrochemically stable window of 3.37 V due to the suppression of water splitting and low overvoltage during the 500 h cycling in a symmetric cell. Zinc dendrites were also suppressed as evidenced in symmetric cell measurements. The assembled AZIB exhibited an initial capacity of 176 mA h g^{-1} upon vertical bending. The battery showed a reliable capacity of 140.7 mA h g^{-1} at 0.2 A g^{-1} after 100 cycles along with a coulombic efficiency of >99%. A reliable capacity of nearly 100 mA h g^{-1} was retained after 300 cycles at 1.0 A g^{-1}. The highly flexible and self-healing AZIB demonstrates great potential in various wearable electronic devices.

Introduction

To date lithium-ion batteries (LIBs) have been widely applied in different fields.[1] However, the use of flammable solvent in electrolyte poses great concerns of safety and cost. Recently rechargeable aqueous Zn-ion batteries (AZIBs) have been of great interest due to their high safety, high theoretical capacity (820 mA h g^{-1}), low electrochemical potential (−0.76 V *vs.* the standard hydrogen electrode), high stability in water, and low cost.[2,3] In order to improve the long-term cycling stability and reduce side reactions such as the hydrogen/oxygen evolution reaction (HER/OER),[4] several strategies have been developed such as Zn metal protection and electrolyte modification.[5] Recently electrolyte additives have attracted a lot of attention.[6] Specific polymer additives can improve the battery flexibility and ductility.[7] The salt-tolerance of polymers is critical in rationally designing hydrogel electrolyte.[8] Due to the better salt compatibility and low cost, a polyacrylamide (PAM) based hydrogel was applied in ZIBs.[9] However, the low stretchability and anti-deformation of the hydrogel can hinder the battery capacity reversibility. In parallel, it is considered that the electrochemical and mechanical properties of the electrolyte would be further improved by forming a dual-network cross-linked hydrogel.[10]

A few cathode materials including vanadium- or manganese-based oxides/sulfides,[11,12] organic materials,[13,14] and Prussian blue analogues (PBAs)[15,16] have been reported in AZIBs.[17] PBA materials have a typical formula of $A_xM[N(CN)_6]_y \cdot nH_2O$ where A presents alkaline metal ions and M and N present transition metals. Due to the unique crystal structure and large interstitial

[a]*Key Laboratory of Functional Molecular Solids, Ministry of Education, College of Chemistry and Materials Science, Anhui Normal University, Wuhu, Anhui 241002, PR China. E-mail: jyliu@ahnu.edu.cn*

[b]*Department of Micro/Nano-Electronics, National Key Laboratory of Science and Technology on Micro/Nano Fabrication, Shanghai Jiao Tong University, Shanghai 200240, PR China*

[c]*Institute of Energy, Hefei Comprehensive National Science Center, Hefei, Anhui 230031, PR China*

[d]*Department of Materials Science and Engineering, University of Wisconsin-Milwaukee, Milwaukee, 53211, Wisconsin, USA. E-mail: niu@uwm.edu*

† Electronic supplementary information (ESI) available. See DOI: https://doi.org/10.1039/d4sc02348j

© 2024 The Author(s). Published by the Royal Society of Chemistry

Open Access Article. Published on 22 May 2024. Downloaded on 2/25/2026 8:18:42 AM.
This article is licensed under a Creative Commons Attribution-NonCommercial 3.0 Unported Licence.

sites, PBAs have attracted a lot of attention in aqueous Li^+, Na^+ and Zn^{2+} ion batteries.[18] However, the combination of Ni/Fe, Cu/Fe or Zn/Fe displays a mono redox reaction pair of Fe(II)/Fe(III) during the charging/discharging process, resulting in a low capacity and a narrow voltage window.[19] The working voltage of most AZIBs is within 1.2 V, which is ascribed not only to the potential difference between the cathode material and Zn metal, but also to the splitting potential of water. Engineering PBA materials with dual-redox reactions is a promising pathway to enhance both the capacity and voltage window.[15,16]

Herein, in order to address the low mechanical strength of the hydrogel electrolyte and low capacity of the PBA cathode material, we developed a highly flexible, self-healing aqueous zinc ion battery by constructing a super-stretchable hybrid hydrogel with polyacrylamide and polyvinyl alcohol (PVA) as electrolyte and PBA cathode material with dual-redox sites of Co(II)/Co(III) and Fe(III)/Fe(II). A large number of hydrogen bonds generated between water molecules and hydroxyl (–OH), amino ($–NH_2$), and carbonyl (C=O) groups on the 3D dual-crosslinked hydrogel framework enable spontaneous healing process at the fracture when cut. The outstanding capacity reversibility of the obtained AZIB during bending and cutting/healing processes was achieved. The self-healed battery still displayed reliable capacities of 119.1, 108.6 and 103.0 mA h g^{-1} even after cutting into 2, 3 and 4 pieces, respectively. In addition, Zn dendrites were largely suppressed by the hybrid electrolyte as evidenced in symmetric cells.

Results and discussion

The as-received cobalt hexacyanoferrate nanoparticles (NPs) have an average size between 40 and 70 nm (Fig. 1a and S1†) and a Brunauer–Emmett–Teller (BET) specific surface area of 98.0 m^2 g^{-1} (Fig. S2†). The Rietveld refinement analysis of the X-ray powder diffraction (XRD) pattern confirmed the PBA crystal structure of $Co_3(Fe(CN)_6)_2 \cdot 10H_2O$ (JCPDS No. 46-0907) (Fig. 1b). It revealed that the sample has an $F\bar{4}3m$ cubic space group and crystal parameters of $a = b = c = 10.266$ Å (Fig. 1b inset). It should be noted that slight diffraction peak deviation could occur due to the lattice distortion by ion insertion. The high-resolution transmission electron microscopy (TEM) image in Fig. 1c shows a d-spacing of 0.512 nm, which is indexed to the (200) plane of $Co_3(Fe(CN)_6)_2 \cdot 10H_2O$. The energy-dispersive spectroscopy (EDS) spectrum confirms the distribution of K, Co, Fe, C and N elements (Fig. S3†). The potassium and lattice water ratios were calculated as $K_{3.24}[Co_3Fe(CN)_6]_2 \cdot 12.6H_2O$ *via* the

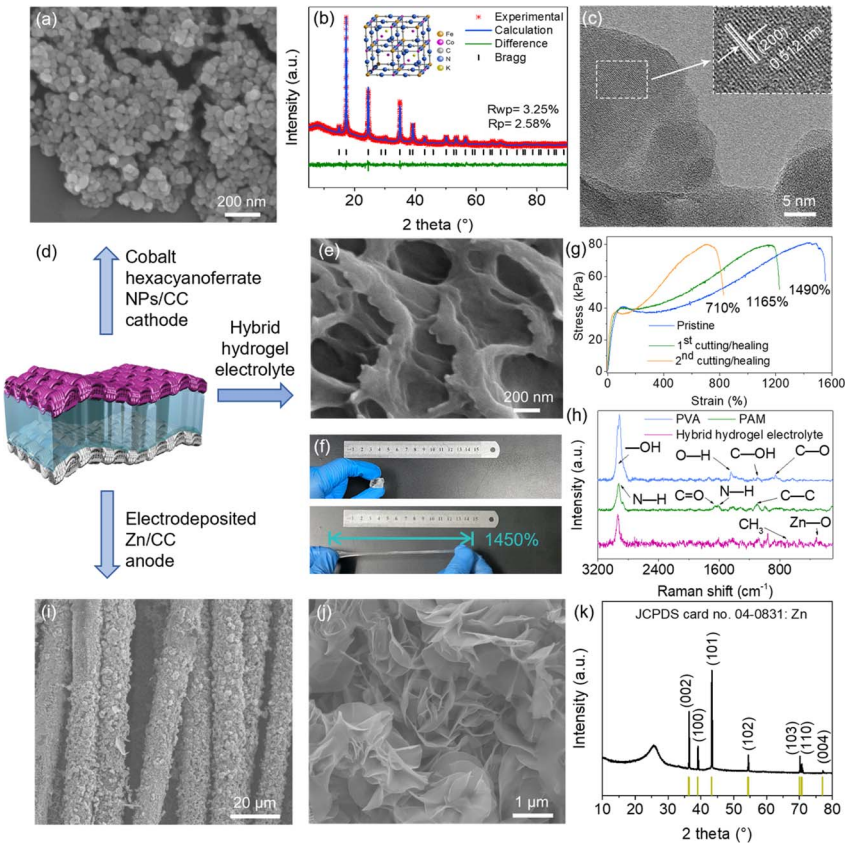

Fig. 1 Design of the quasi-solid-state AZIB. (a) Scanning electron microscopy (SEM) image and (b) XRD Rietveld refinement results of the as-received cobalt hexacyanoferrate NPs. The inset of (b) shows the crystal structure with the cell parameters of $a = b = c = 10.266$ Å viewed from the [111] direction. (c) High-resolution TEM image of a cobalt hexacyanoferrate NP. (d) Schematical illustration of the quasi-solid-state AZIB using cobalt hexacyanoferrate NPs/CC as the cathode, Zn/CC as the anode, and the hybrid hydrogel as the electrolyte. (e) SEM morphology of freeze-dried hydrogel electrolyte. (f) Stretching performance of the hydrogel. (g) Tensile tests of the hydrogel after two cutting-healing cycles. (h) Raman spectra of the freeze-dried hydrogel electrolyte. (i) Low- and (j) high-magnification SEM images and (k) XRD pattern of electrodeposited Zn/CC.

Open Access Article. Published on 22 May 2024. Downloaded on 2/25/2026 8:18:42 AM. This article is licensed under a Creative Commons Attribution-NonCommercial 3.0 Unported Licence.

mass loss and composition of residues by using thermogravimetry analysis (TGA) (Fig. S4†). In parallel, the chemical state of cobalt hexacyanoferrate was analysed by X-ray photoelectron spectroscopy (XPS), as shown in Fig. S5.† Two peaks at 286.3 and 288.7 eV which correspond to C≡N and C=O from the adsorbed CO_2 were observed (Fig. S5b†).[20] The peaks at 296.5 and 293.7 eV are attributed to K $2p_{1/2}$ and K $2p_{3/2}$, respectively.[21] The Co $2p_{1/2}$ peak at 797.4 eV and Co $2p_{3/2}$ peak at 782.2 eV demonstrate the existence of Co^{3+} (Fig. S5c†).[22] The peaks at 800.7 and 784.9 eV with two satellite peaks at 788.3 and 803.7 eV indicate the existing Co^{2+}.[23] In Fig. S5d,† the peaks at 721.2 and 708.4 eV are assigned to Fe $2p_{1/2}$ and Fe $2p_{1/2}$, indicating the presence of Fe^{3+}, while the peaks at 723.4 and 709.9 eV are related to Fe^{2+}.[24] The bindings of C≡N and C–N were confirmed by the two peaks at 398.6 and 397.8 eV (Fig. S5e†).[25]

In order to enhance the mechanical properties of the hydrogel, different mass ratios of PAM and the PVA additive were applied to form the dual-network composite (Fig. S6†). As shown in Fig. 1e, the hybrid hydrogel electrolyte presents a porous structure with 57.1% water, which is beneficial for electrolyte penetration and Zn^{2+} ion migration.[26] The hydrogel with the acrylamide (AM) monomer below 1.0 g exhibited low mechanical strength, and is unable to confine the liquid electrolyte. The electrolyte became robust when the AM monomer reached 3.0 g (Fig. S7†). The dense configuration with less water was not favourable for Zn^{2+} migration. The hybrid hydrogel electrolyte displayed an ionic conductivity of 6.7 mS cm^{-1}, compared to 34.1 mS cm^{-1} of the liquid electrolyte (Fig. S8†). The confined Zn^{2+} ions by the hydrophilic groups in the polymer led to decreased ionic conductivity.[27] The hydrogel obtained with a PVA : AM mass ratio of 0.5 : 2.0 displayed an ultrahigh strain of up to 1450% before failure (Fig. 1f). The self-healed hydrogel after cutting a 1.0 inch × 1.0 inch hydrogel into several pieces still showed a high strain of 1165% and 710% after two and three cutting/healing cycles (Fig. 1g and S9†). The functional groups of the freeze-dried hybrid electrolyte, commercial PAM and PVA were investigated through Raman spectroscopy. As shown in Fig. 1h, four Raman peaks at 2916, 1450, 1100 and 857 cm^{-1} correspond to commercial PVA, and are assigned to the vibration of –OH, –OH, C–OH and C–O, respectively.[28] For PAM, the peaks at 2928, 1667, 1615 and 1100 cm^{-1} are ascribed to N–H stretching, C=O stretching, N–H bending and C–C skeletal stretching vibration, respectively.[29] Two new peaks appear at 697 and 332 cm^{-1} with the hybrid hydrogel electrolyte, which are respectively indexed to the CH_3 deformation and Zn–O vibrations, indicating the presence of zinc acetate.[30,31] In parallel, the peak located at 1022 cm^{-1} and a series of peaks at 752–458 cm^{-1} confirm the vibration of CH_3COO^- and Zn–O–Zn from the hybrid hydrogel electrolyte (Fig. S10†). The abundant amino ($-NH_2$), hydroxyl (–OH), and carbonyl (C=O) groups in the hybrid electrolyte might avoid electrolyte crossover and enhance the wettability at the interface between the electrolyte and electrode.[32] These functional groups lead to the formation of hydrogen bonds in an aqueous environment, showing outstanding self-healing performance.[33] When the broken pieces were re-connected, plenty of new hydrogen bonds were regenerated between the functional groups and water molecules which exist on the fractured interfaces. In addition to the PBA cathode and hydrogel electrolyte, Zn electrodeposited on carbon cloth (CC) was applied as the anode electrode (Fig. 1d). It is shown that high-density flower-shaped Zn nanosheets were deposited on the carbon fibers (Fig. 1i and j). The XRD pattern confirms the high purity of crystal Zn (Fig. 1k).

The cycling stability of water-based electrolyte with a suitable potential window is important for long-term battery cycling performance. In Fig. 2a, the liquid electrolyte shows an electrochemically stable potential window of 2.18 V (−0.86–1.32 V *vs.* Ag/AgCl), while the hybrid electrolyte delivers an expanded window of 2.69 V (−0.97–1.72 V *vs.* Ag/AgCl). This is attributed to the suppression of active water molecules by the PAM/PVA crosslinked framework, which enables Zn deposition/stripping prior to electrochemical splitting of water upon cycling.

The Zn deposition/stripping behaviours were investigated by using Zn‖Zn symmetric cells. The cell with hydrogel electrolyte at 1.0 mA cm^{-2} and 1.0 mA h cm^{-2} with a depth of discharge (DOD) of 16.7% was stably cycled for 500 hours, while the cell with liquid electrolyte showed a larger overvoltage and variation (Fig. 2b). During the Zn‖Cu asymmetric cell test at 1.0 mA cm^{-2} and 1.0 mA h cm^{-2}, the hydrogel electrolyte showed a high coulombic efficiency (CE) of 99.1% and a smooth potential after 300 cycles (Fig. 2c and d). However, the liquid electrolyte exhibited a drastic decrease after 65 cycles (Fig. 2c, d and S11†), which is ascribed to the irreversible Zn plating and possible formation of dendrites. The uniform Zn deposition/extraction may be attributed to the high energy barrier of Zn^{2+} ion nucleation and confined diffusion, which is due to the coordination between Zn^{2+} ions and abundant acylamino and hydroxyl groups on the PAM–PVA framework.[34,35] In order to investigate the Zn plating behavior, both liquid and hydrogel electrolytes were cycled at a high current density of 75 mA cm^{-2}. As seen in Fig. 2e, S12a and Movie S1,† Zn started to grow and formed protrusions/mossy zinc after 30 s in the liquid electrolyte. This irregular growth of zinc results in forming 'dead zinc' during the stripping process, which decreases the overall capacity and cyclability. As a comparison, the Zn plate with hydrogel as electrolyte delivered uniform deposition and stripping of zinc during the cycling process (Fig. 2f, S12b and Movie S2†).

The electrochemical properties and battery cycling performance were investigated by constructing a quasi-solid-state AZIB by using the hybrid hydrogel as electrolyte and cobalt hexacyanoferrate NPs/CC and Zn/CC as the cathode and anode, respectively (Fig. 1d). As seen in Fig. 3a, cyclic voltammetry (CV) curves of the battery with a scanning rate of 0.1 mV s^{-1} show better reversibility during the 5 cycles. Two cathodic peaks appear at 1.45 V and 1.62 V, and correspond to the Fe(III) → Fe(II) and Co(III) → Co(II) reductions along with Zn^{2+} intercalation, while the anodic peak at 1.84 V originates from both Fe(II) → Fe(III) and Co(II) → Co(III) during Zn^{2+} deintercalation.[36] Fig. 3b shows CV curves at scanning rates from 0.1 to 1.0 mV s^{-1}. The scanning rate and peak current follow an empirical law of $i = av^b$,[37] which is usually transformed into $\log(i) = b\log(v) + \log(a)$, where the b value refers to the slope value obtained by plotting log(v, scanning rate) and log(i, peak

© 2024 The Author(s). Published by the Royal Society of Chemistry

Open Access Article. Published on 22 May 2024. Downloaded on 2/25/2026 8:18:42 AM. This article is licensed under a Creative Commons Attribution-NonCommercial 3.0 Unported Licence.

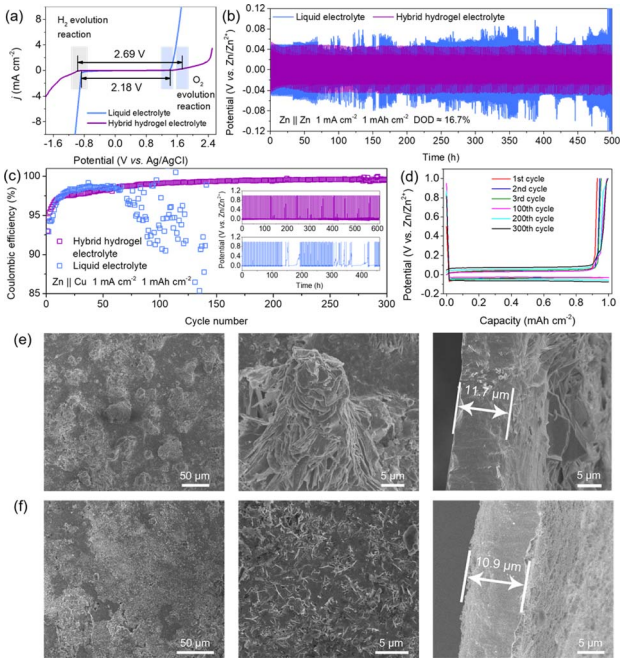

Fig. 2 Comparison of the hybrid hydrogel and liquid electrolytes. (a) Electrochemically stable potential window *via* linear sweep voltammetry (LSV) measurement. (b) Cycling performance of Zn||Zn symmetric cells. (c) The cycling performance of Zn||Cu asymmetric cells and (d) the corresponding polarization. SEM morphologies of Zn plating with (e) liquid and (f) hybrid hydrogel electrolytes at a current density of 75 mA cm^{-2} and capacity of 75 mA h cm^{-2}.

current). The calculated *b* value of peak 1 and peak 2 is 0.976 and 0.550, which indicates both faradaic (diffusion-controlled) and non-faradaic (surface controlled capacitive behavior) processes (Fig. S13†).[38] The dominant surface controlled capacitive behavior was confirmed by using the contribution ratio at varying scanning rates (Fig. 3c). As a comparison, the battery with liquid electrolyte showed a diffusion-controlled faradaic process (Fig. S14†), which is detrimental for the long-term stability particularly at high current densities.[39]

The galvanostatic charging/discharging (GCD) results of the AZIB with hydrogel electrolyte are shown in Fig. 3d. The plateau at about 1.6 V during the discharging process corresponds to the reduction of Fe(III) and Co(III) to Fe(II) and Co(II) during Zn^{2+} intercalation, while the plateau at around 1.8 V is assigned to the regeneration of Fe(III) and Co(III) during Zn^{2+} extraction.[40] The assembled battery still showed a high capacity of 140.7 mA h g^{-1} along with a CE of >99% after 100 cycles at 0.2 A g^{-1} (Fig. 3e). In contrast, the battery with liquid electrolyte only showed a capacity of 66.9 mA h g^{-1} after 100 cycles. The rapid capacity decay was mainly caused by a series of side reactions which formed by-products such as ZnO and $Zn(OH)_2$. The consumption of water resulted in poor electrolyte contact with the cathode and anode. The formation of zinc salts prevented the deintercalation of Zn^{2+}, leading to irreversible capacity loss. The low initial CE is attributed to the dissolution of lattice K^+ during the charging process (Fig. 4e).[41] The battery with the hybrid hydrogel electrolyte also displayed better rate-performance at varying current densities (Fig. S15†). The cycling performance at a high current density of 1.0 A g^{-1} is shown in Fig. 3f. It was found that the battery with hydrogel electrolyte displayed an initial capacity of 125.9 mA h g^{-1}, which is similar to the battery with liquid electrolyte. A capacity of nearly 100.0 mA h g^{-1} along with a high CE of 99.9% after 300 long cycles was still retained while the capacity of the battery with liquid electrolyte decreased to 59.8 mA h g^{-1} after only 60 cycles.

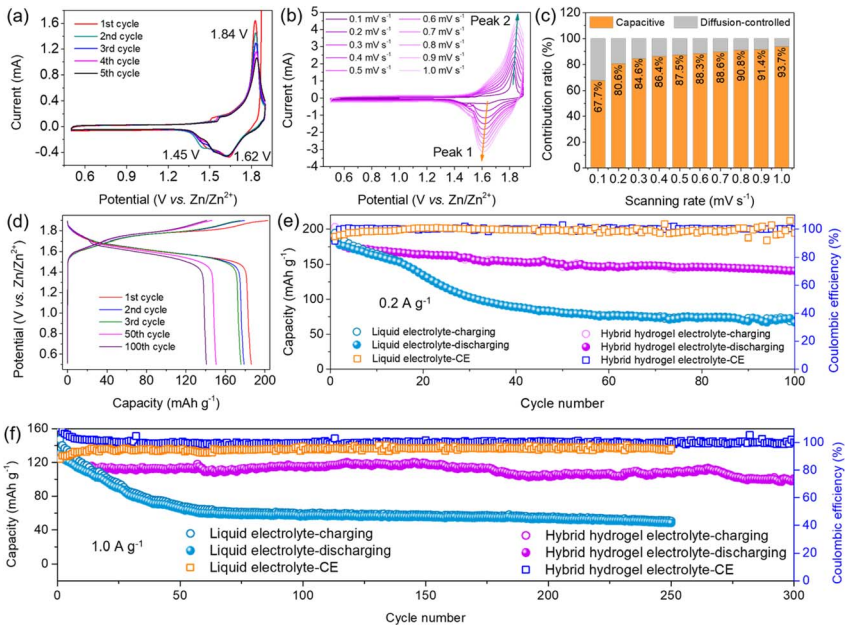

Fig. 3 Electrochemical properties and battery performance of the assembled AZIBs. (a) CV curves at a scanning rate of 0.1 mV s^{-1}. (b) CV curves at a scanning rate ranging from 0.1 to 1.0 mV s^{-1}. (c) Capacitive and diffusion-controlled ratios obtained from CV peaks. (d) GCD curves. (e) Battery cycling performance at 0.2 A g^{-1}. (f) Long-term cycling performance at a current density of 1.0 A g^{-1}.

© 2024 The Author(s). Published by the Royal Society of Chemistry

Open Access Article. Published on 22 May 2024. Downloaded on 2/25/2026 8:18:42 AM.
This article is licensed under a Creative Commons Attribution-NonCommercial 3.0 Unported Licence.

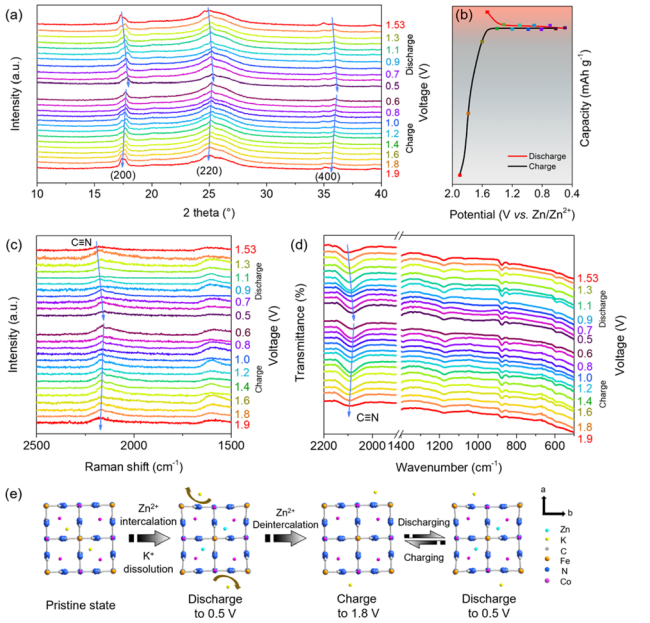

Fig. 4 Mechanism study of the cobalt hexacyanoferrate cathode at various potentials within one cycle. (a) *Ex situ* XRD patterns and (b) the corresponding GCD curve. *Ex situ* (c) Raman and (d) ATR-FTIR spectra. (e) Schematic illustration of the Zn-storage mechanism in cobalt hexacyanoferrate.

It is believed that the hydrogel electrolyte successfully suppressed the side reactions and K^+ dissolution even at high current density.

Galvanostatic intermittent titration technique (GITT) measurements were performed at a current density of 0.1 A g^{-1} (Fig. S16a†) with both pulse and relaxion times of 600 s (Fig. S16b†). The diffusion coefficient of Zn^{2+} and the internal reaction resistance were evaluated according to Fick's law.[42] As shown in Fig. S16c,† the battery with hydrogel electrolyte delivered a reaction resistance from 9.22 × 10^4 to 1.32 × 10^6 Ω g^{-1} when discharging from 1.76 to 0.5 V, while the battery with liquid electrolyte exhibited a larger resistance from 6.21 × 10^5 to 2.41 × 10^6 Ω g^{-1}. In the subsequent charging process, the resistance was decreased to 8.73 × 10^4 Ω g^{-1} while the battery with liquid electrolyte still has a resistance of 5.36 × 10^5 Ω g^{-1} on charging to 1.9 V.

The Zn-storage mechanism was studied by *ex situ* XRD, *ex situ* Raman spectroscopy and attenuated total reflection FTIR (ATR-FTIR). As displayed in Fig. 4a and b, the diffraction peaks of the (200), (220) and (400) planes positively shifted when the battery was discharged to 0.5 V, indicating the reducing interplanar spacing due to Zn^{2+} intercalation. This lattice contraction was from the smaller radius of $[Fe(II)(CN)_6]^{4-}$ that was transformed from $[Fe(III)(CN)_6]^{3-}$.[43] During the charging process, these peaks were recovered, indicating high reversibility of Zn^{2+} intercalation/deintercalation in cobalt hexacyanoferrate. A strong peak at 2176 cm^{-1} corresponds to the vibration of C≡N of cobalt hexacyanoferrate, while the peaks at around 513 cm^{-1} match the vibration of Co–N and Fe–C in the Raman spectrum (Fig. S17a†). The peak at 2115 cm^{-1} in the ATR-FTIR spectrum is indexed to the vibration of C≡N (Fig. S17b†).[44,45] As observed in Fig. 4c, the C≡N peak showed a red shift when the battery was discharged to 0.5 V, which was due to the gradual reduction of N-coordinated Co^{3+} ions along with Zn^{2+} intercalation.[46] During charging, this peak shifted back to the original position upon Zn^{2+} ion extraction. A similar evolution was also observed from the *ex situ* ATR-FTIR spectra (Fig. 4d), which was ascribed to the influence on the electron distribution of carbon and nitrogen atoms by the redox pairs of Fe(II)/Fe(III) and Co(II)/Co(III) during Zn^{2+} intercalation/extraction.[47] The Zn-storage mechanism of cobalt hexacyanoferrate is illustrated in Fig. 4e. The existing K^+ ions from the prime state were dissolved in the electrolyte at the initial charging/discharging, which led to lattice contraction and distortion. In the successive cycles, most K^+ ions were unable to return back to the original sites, thus leaving Zn^{2+} ions to be reversibly inserted and extracted in the K-deficient state.[48] The lower intensity of the K signal of the post-cycled cobalt hexacyanoferrate was observed from the EDS spectra (Fig. S18†).

The mechanical flexibility and self-healing properties of the assembled quasi-solid-state AZIB were investigated. As illustrated in Fig. 5a, the battery still showed initial capacities of 181.3 and 176.0 mA h g^{-1} after bending 30 times at 60° and 90°, respectively. A high capacity retention of 113.6 and 98.4 mA h

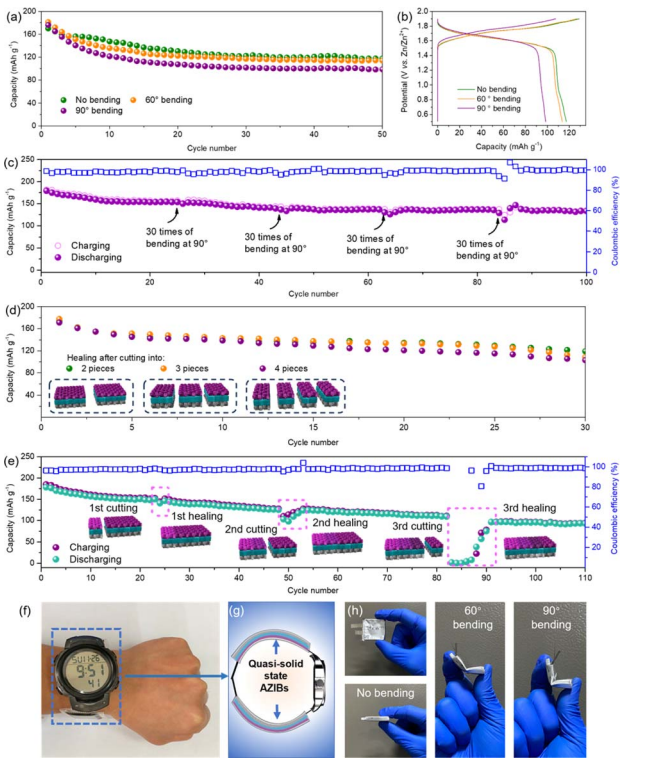

Fig. 5 Self-healing performance of the quasi-solid-state AZIB. (a) Cycling performance and (b) GCD curves upon bending after 50 cycles. (c) Electrochemical performance of the battery after four rounds of bending 30 times at 90°. (d) Capacity retention of the battery after self-healing from cutting into 2, 3 and 4 pieces. (e) Electrochemical performance of the battery during three cutting/healing cycles. (f) Optical photograph and (g) illustration of a watch powered by two assembled AZIBs. (h) Optical photographs of the battery before and after bending 30 times at 60° and 90°, respectively.

© 2024 The Author(s). Published by the Royal Society of Chemistry

Open Access Article. Published on 22 May 2024. Downloaded on 2/25/2026 8:18:42 AM. This article is licensed under a Creative Commons Attribution-NonCommercial 3.0 Unported Licence.

g^{-1} along with a flat voltage plateau was observed after 50 cycles (Fig. 5b). The battery displayed high capacity retention of 99.5%, 99.8%, 98.6% and 98.9% in contrast to the capacity before bending even after four rounds of bending 30 times at 90° (Fig. 5c). Self-healing performance of the battery was investigated by cutting the battery into a few pieces. As seen in Fig. 5d, the self-healed battery still delivered a high capacity of 119.1, 108.6 and 103.0 mA h g^{-1} after 30 continuous cycles after cutting into 2, 3 and 4 pieces, respectively. Furthermore, the recovered battery after three successive cutting/healing cycles retained a high capacity of 96.5 mA h g^{-1} along with a recovery rate of 88.2% after 110 cycles (Fig. 5e). The battery capacity gradually stabilized at 146.3 and 123.7 mA h g^{-1} with a recovery rate of 98.7% and 98.3% after the first and second cutting/healing cycles, respectively, indicating good self-healing and capacity recovery performance. In addition, it was found that the open circuit voltage retention rate of the battery is as high as 91.3%, 87.2%, 76.3% and 75.3%, respectively, after four cutting/healing cycles (Fig. S19†). This result implies a better voltage recovery capability even after severe destruction. As a comparison, the battery with pure PAM electrolyte showed fast capacity decay under bending or cutting/healing (Fig. S20†), implying low flexibility and less self-healing properties. As demonstrated in Fig. 5f and g, two AZIBs were connected in series to supply power for an electric watch. Due to the better twisting (Fig. S21a and b†), compression (Fig. S21c and d†) and bending performance at different angles (Fig. 5h), the AZIB shows high compatibility with flexible motion of the wrist.

Conclusions

In summary, a quasi-solid-state self-healing aqueous zinc-ion battery was developed by using a hybrid hydrogel as the electrolyte and Prussian blue analogue cobalt hexacyanoferrate as the cathode material. On the basis of excellent wettability and abundant hydrogen bonds between hydroxyl, amino, and carbonyl groups on the hydrogel framework and water molecules, the assembled battery showed excellent mechanical-electro-chemo flexibility and self-healing properties. The self-healed battery still displayed high-capacity retention after being cut into a few pieces. After four rounds of bending 30 times at 90°, the battery delivered a >98.6% high-capacity recovery rate. Furthermore, the hydrogel electrolyte displayed a wide potential window of 3.37 V due to the suppression of water splitting and side reactions. The obtained battery showed a reliable capacity of about 100 mA h g^{-1} after 300 cycles at a high current density of 1.0 A g^{-1}. The outstanding flexibility and self-healing properties upon bending/cutting make it favorable in various wearable and foldable electronic devices.

Author contributions

J. Y. L. conceived the project and wrote the manuscript. J. W. L. performed the characterization and performance tests. T. L. H, X. R. L. and Y. J. Z. participated the experiments and data analysis. J. J. N. revised the manuscript.

Conflicts of interest

There are no conflicts to declare.

Acknowledgements

This work was supported by the Major Science and Technology Research Project of Anhui Province (2023z020003), the Key Research and Development Program of Wuhu (2022YF53), Cooperation Funding for Long Cycle Life and High-Capacity Battery Materials (901/852309), Anhui Provincial Quality Engineering for Cooperative Practice Education Base (2022xqhz020), and the Natural Science Research Project for Universities in Anhui Province (2022AH050176).

Notes and references

1 H. Wan, J. Xu and C. Wang, *Nat. Rev. Chem.*, 2024, **8**, 30–44.
2 T. Wang, Y. Zhang, J. You and F. Hu, *Chem. Rec.*, 2023, **23**, e202200309.
3 C. Nie, G. Wang, D. Wang, M. Wang, X. Gao, Z. Bai, N. Wang, J. Yang, Z. Xing and S. Dou, *Adv. Energy Mater.*, 2023, **13**, 2300606.
4 J. Chen, W. Zhao, J. Jiang, X. Zhao, S. Zheng, Z. Pan and X. Yang, *Energy Storage Mater.*, 2023, **59**, 102767.
5 Z. Zhang, Z. He, N. Wang, F. Wang, C. Du, J. Ruan, Q. Li, D. Sun, F. Fang and F. Wang, *Adv. Funct. Mater.*, 2023, **33**, 2214648.
6 Y. Li, H. Yao, X. Liu, X. Yang and D. Yuan, *Nano Res.*, 2023, **16**, 9179–9194.
7 M. Han, T. Li, D. Li and H. Yang, *Batteries Supercaps*, 2023, **6**, e202200560.
8 C. Wang, X. Zeng, J. Qu, J. M. Cairney, Q. Meng, P. J. Cullen and Z. Pei, *Matter*, 2023, **6**, 3993–4012.
9 N. Sun, H. Sun, D. Tan, Q. Guo, Z. Zhang, Z. Tao, C. Fang, J. Bu, J. Huang and C. Jiang, *Chem. Eng. J.*, 2023, **469**, 143997.
10 R. Takahashi, K. Shimano, H. Okazaki, T. Kurokawa, T. Nakajima, T. Nonoyama, D. R. King and J. P. Gong, *Adv. Mater. Interfaces*, 2018, **5**, 1801018.
11 Y. Dai, C. Zhang, J. Li, X. Gao, P. Hu, C. Ye, H. He, J. Zhu, W. Zhang, R. Chen, W. Zong, F. Guo, I. P. Parkin, D. J. L. Brett, P. R. Shearing, L. Mai and G. He, *Adv. Mater.*, 2024, **36**, 2310645.
12 Y. Li, Y. Li, Q. Liu, Y. Liu, T. Wang, M. Cui, Y. Ding, H. Li and G. Yu, *Angew. Chem., Int. Ed.*, 2024, **63**, e202318444.
13 L. Huang, J. Li, X. Gao, J. Wang, H. Lv, H. Xie, Y. Liu, T. Gu and G. Wang, *J. Power Sources*, 2024, **591**, 233896.
14 M. Cheng, S. Zheng, T. Sun, D. Li, W. Zhang, Z. Zha, Q. Sun, J. Tian, K. Zhang and Z. Tao, *Nano Res.*, 2024, DOI: **10.1007/s12274-12023-16401-12278**.
15 T. Yuan, Y. Chen, X. Gao, R. Xu, Z. Zhang, X. Chen and L. Cui, *Small Methods*, 2023, DOI: **10.1002/smtd.202301372**.
16 J. Liu, Z. Shen and C. Lu, *J. Mater. Chem. A*, 2024, **12**, 2647–2672.
17 G. Li, L. Sun, S. Zhang, C. Zhang, H. Jin, K. Davey, G. Liang, S. Liu, J. Mao and Z. Guo, *Adv. Funct. Mater.*, 2024, **34**, 2301291.

Open Access Article. Published on 22 May 2024. Downloaded on 2/25/2026 8:18:42 AM. This article is licensed under a Creative Commons Attribution-NonCommercial 3.0 Unported Licence.

18 J. Peng, W. Zhang, Q. Liu, J. Wang, S. Chou, H. Liu and S. Dou, *Adv. Mater.*, 2022, **34**, 2108384.
19 Y. Li, J. Zhao, Q. Hu, T. Hao, H. Cao, X. Huang, Y. Liu, Y. Zhang, D. Lin, Y. Tang and Y. Cai, *Mater. Today Energy*, 2022, **29**, 101095.
20 Y. Wang, Z. Gong, Y. Zeng, H. Zhao and J. Yang, *Chem. Eng. J.*, 2022, **431**, 134066.
21 C. Zhang, J. Chen, X. Yin, Y. Sun, W. Yang, F. Yu, X. Liu, L. Fu, Y. Chen and Y. Wu, *Chem. Commun.*, 2021, **57**, 1607–1610.
22 D. Pal, D. Maity, A. Sarkar, D. De, A. Raj and G. G. Khan, *ACS Appl. Energy Mater.*, 2022, **5**, 15000–15009.
23 H. Xie, K. Wang, D. Xiang, S. Li and Z. Jin, *J. Mater. Chem. A*, 2023, **11**, 14971–14989.
24 J. Ma, Y. Li, X. Wei, Z. Li, G. Li, T. Liu, Y. Zhao, S. He, Y. Li, R. Li, C. Gu, J. Li, H. Luo, Q. Wang, K. Li and C. Liu, *Chem. Eng. J.*, 2022, **433**, 133777.
25 W. Hou, C. Yan, P. Shao, K. Dai and J. Yang, *Nanoscale*, 2022, **14**, 8501–8509.
26 C. Wang, Z. Pei, Q. Meng, C. Zhang, X. Sui, Z. Yuan, S. Wang and Y. Chen, *Angew. Chem., Int. Ed.*, 2021, **60**, 990–997.
27 Y. Wang, Q. Li, H. Hong, S. Yang, R. Zhang, X. Wang, X. Jin, B. Xiong, S. Bai and C. Zhi, *Nat. Commun.*, 2023, **14**, 3890.
28 J. C. Bonafé Allende, R. N. Schmarsow, E. Matxinandiarena, S. D. García Schejtman, E. A. Coronado, C. I. AlvarezIgarzabal, M. L. Picchio and A. J. Müller, *Macromolecules*, 2022, **55**, 10870–10879.
29 Y. Zhou, S. Zhang, M. A. Buckingham, L. Aldous, S. Beirne, C. Wu, Y. Liu, G. Wallace and J. Chen, *Chem. Eng. J.*, 2022, **449**, 137775.
30 B. Huang, Q. Zhao, C. Sun, L. Zhu, H. Xu, Y. Zhang and F. Li, *Food Chem.*, 2023, **429**, 136851.
31 K. Geetha, D. Sivasangari, H. Kim, G. Murugadoss and A. Kathalingam, *Ceram. Int.*, 2022, **48**, 29197–29204.
32 H. Lim, S. Chae, L. Yan, G. Li, R. Feng, Y. Shin, Z. Nie, B. M. Sivakumar, X. Zhang, Y. Liang, D. J. Bazak, V. Shutthanandan, V. Murugesan, S. Kim and W. Wang, *Energy Mater. Adv.*, 2022, **2022**, 9863679.
33 X. Cui, C. Wang, W. Huang, S. Zhang, H. Chen, B. Wu, D. Qin and X. Zheng, *ACS Omega*, 2023, **8**, 39401–39407.
34 Y. Wang, L. Yang, P. Xu, L. Liu, S. Li, Y. Zhao, R. Qin and F. Pan, *Small*, 2024, **20**, 2307446.
35 X. Chen, W. Li, S. Hu, N. G. Akhmedov, D. Reed, X. Li and X. Liu, *Nano Energy*, 2022, **98**, 107269.
36 L. Ma, S. Chen, C. Long, X. Li, Y. Zhao, Z. Liu, Z. Huang, B. Dong, J. A. Zapien and C. Zhi, *Adv. Energy Mater.*, 2019, **9**, 1902446.
37 H. Li, K. Fan, P. Xiong, H. Zhou, Z. Lin, K. Tao, T. Liu, X. Guo, Y. Zhu, L. Zhuang, W. Han, C. Yang, Y. Liu, M. MengJung Li, M. Fu, J. Wang and H. Huang, *J. Mater. Chem. A*, 2024, **12**, 3449–3459.
38 W. Zhang, Y. Wu, Z. Xu, H. Li, M. Xu, J. Li, Y. Dai, W. Zong, R. Chen, L. He, Z. Zhang, D. J. L. Brett, G. He, Y. Lai and I. P. Parkin, *Adv. Energy Mater.*, 2022, **12**, 2201065.
39 X. Zhu, Q. She, M. Wang, Z. Wang, Y. Hu, D. Yuan, Y. Sun, T. U. Schülli and L. Wang, *Adv. Funct. Mater.*, 2024, **34**, 2311025.
40 L. Ma, S. Chen, N. Li, Z. Liu, Z. Tang, J. A. Zapien, S. Chen, J. Fan and C. Zhi, *Adv. Mater.*, 2020, **32**, 1908121.
41 H. Ao, W. Zhu, M. Liu, W. Zhang, Z. Hou, X. Wu, Y. Zhu and Y. Qian, *Small Methods*, 2021, **5**, 2100418.
42 Y. Chien, H. Liu, A. S. Menon, W. R. Brant, D. Brandell and M. J. Lacey, *Nat. Commun.*, 2023, **14**, 2289.
43 Z. Liu, G. Pulletikurthi and F. Endres, *ACS Appl. Mater. Interfaces*, 2016, **8**, 12158–12164.
44 W. O. Silva, V. Costa Bassetto, D. Baster, M. Mensi, E. Oveisi and H. H. Girault, *ACS Appl. Electron. Mater.*, 2020, **2**, 927–935.
45 X. Zhang, L. Tao, P. He, X. Zhang, M. He, F. Dong, S. He, C. Li, H. Liu, S. Wang and Y. Zhang, *Electrochim. Acta*, 2018, **259**, 793–802.
46 D. Luo, P. Lei, G. Tian, Y. Huang, X. Ren and X. Xiang, *J. Phys. Chem. C*, 2020, **124**, 5958–5965.
47 W. Ren, Z. Zhu, M. Qin, S. Chen, X. Yao, Q. Li, X. Xu, Q. Wei, L. Mai and C. Zhao, *Adv. Funct. Mater.*, 2019, **29**, 1806405.
48 T. Cao, F. Zhang, M. Chen, T. Shao, Z. Li, Q. Xu, D. Cheng, H. Liu and Y. Xia, *ACS Appl. Mater. Interfaces*, 2021, **13**, 26924–26935.

© 2024 The Author(s). Published by the Royal Society of Chemistry